

# Intercalation-conversion hybrid cathodes enabling Li-S full-cell architectures with jointly superior gravimetric and volumetric energy densities

Weijiang Xue<sup>1</sup>, Zhe Shi<sup>1</sup>, Liumin Suo<sup>1,2,3,4\*</sup>, Chao Wang<sup>1</sup>, Ziqiang Wang<sup>1</sup>, Haozhe Wang<sup>1,5</sup>, Kang Pyo So<sup>1</sup>, Andrea Maurano<sup>1,6</sup>, Daiwei Yu<sup>5</sup>, Yuming Chen<sup>1</sup>, Long Qie<sup>1,7</sup>, Zhi Zhu<sup>1</sup>, Guiyin Xu<sup>1</sup>, Jing Kong<sup>5</sup> and Ju Li<sup>1\*</sup>

**A common practise in the research of Li-S batteries is to use high electrode porosity and excessive electrolytes to boost sulfur-specific capacity. Here we propose a class of dense intercalation-conversion hybrid cathodes by combining intercalation-type  $\text{Mo}_6\text{S}_8$  with conversion-type sulfur to realize a Li-S full cell. The mechanically hard  $\text{Mo}_6\text{S}_8$  with fast Li-ion transport ability, high electronic conductivity, active capacity contribution and high affinity for lithium polysulfides is shown to be an ideal backbone to immobilize the sulfur species and unlock their high gravimetric capacity. Cycling stability and rate capability are reported under realistic conditions of low carbon content (~10 wt%), low electrolyte/active material ratio (~1.2  $\mu\text{L mg}^{-1}$ ), low cathode porosity (~55 vol%) and high mass loading (>10  $\text{mg cm}^{-2}$ ). A pouch cell assembled based on the hybrid cathode and a 2× excess Li metal anode is able to simultaneously deliver a gravimetric energy density of 366  $\text{Wh kg}^{-1}$  and a volumetric energy density of 581  $\text{Wh l}^{-1}$ .**

Anion-redox lithium-sulfur (Li-S) is one of the most promising conversion battery chemistries with high theoretical cathode energy density of 2,600  $\text{Wh kg}^{-1}$  based on the weight of  $\text{Li}_2\text{S}$ ,  $\text{S}_8 + 16\text{e}^- + 16\text{Li}^+ = 8\text{Li}_2\text{S}$ , several times higher than conventional lithium-ion battery (LIB) cathodes based on transition metal cation-redox intercalation reactions<sup>1,2</sup>. Unfortunately, the actual full-cell energy densities are a far cry from the theoretical values resulting from the excessive use of inactive components, such as electrolyte and conductive carbon. The electronic insulating nature of the  $\text{S}_8$  and  $\text{Li}_2\text{S}$  phases (as compared to, say,  $\text{Li}_x\text{CoO}_2$ , with its high  $\text{Co}^{3+} \leftrightarrow \text{Co}^{4+}$  polaron mobility) means that for the anion-redox reaction  $\text{S}^{\alpha-} \leftrightarrow \text{S}^{\beta-} + (\alpha - \beta)\text{e}^-$  to proceed (where  $0 \leq \alpha, \beta \leq 2$  is the average sulfur valence reflecting a mix of ionic and covalent bonding, often in the physical form of  $\text{S}_n^{2-}$ , where  $\alpha = 2/n$ ), the  $\text{S}_8$  must physically dissolve into liquid electrolytes as  $\text{S}_n^{2-}$  (electrolyte), transform into  $\text{S}_m^{2-}$  (electrolyte) and eventually redeposit somewhere else as solid phases.

This sulfur mobility is a key characteristic of many Li-S batteries, which has profound consequences on battery processes and performances. First, the dissolution of lithium polysulfide intermediates (LiPS) in the liquid electrolyte does help the kinetics. Even though LiPS is often written as  $\text{Li}_2\text{S}_n$ , one needs to understand that its solubilized form is  $2\text{Li}^+$  (electrolyte) and  $\text{S}_n^{2-}$  (electrolyte), with individual solvation shells. A problem brought by such sulfur mobility is that  $\text{S}_n^{2-}$  (electrolyte) may physically cross over the separator to the Li metal anode in a non-blocking manner (so-called ‘shuttling’ of soluble redox mediators). This causes fast capacity fading on the

cathode side, even if we do not consider the ill effects this has on the anode<sup>3</sup>. Second, to enhance the sluggish redox kinetics of  $\text{S}_8 \leftrightarrow \text{Li}_2\text{S}$ , one needs a lot more liquid electrolyte and electrocatalytical surface areas in the cathode, which can be a common carbon black (which is neither a particularly good electrocatalyst, nor a good wetting substrate), or something more tailor made. Although a high fraction of conductive carbons (>30 wt%)<sup>4</sup> is usually required for sufficient sulfur use in conventional C/ $\text{S}_8$  cathodes, it is equally true that such an excessive use (compared to LIB cathodes with 5 wt% carbon) of high-specific-area carbons gives rise to high cathode porosity (usually >70 vol%)<sup>5</sup>, which demands a considerable amount of electrolyte to support a satisfactory ionic conductivity<sup>6</sup>. The theoretical prediction for the relationship between cathode porosity and cathode-specific energy densities in Fig. 1 shows that the porosity greatly affects both the cathode-specific gravimetric  $e_g$  and volumetric  $e_v$  energy densities. In most studies, a high electrolyte to active material ratio (E/AM ratio) >15  $\mu\text{L mg}^{-1}$  (ref. 7) (~0.3  $\mu\text{L mg}^{-1}$  for LIB cathode) is employed<sup>8</sup>. In other words, the most impressive high specific capacity based on just the  $\text{S}_8$  weight is attained with a large excess of cathode porosity and electrolyte. In this case, the full-cell gravimetric  $E_g$  and volumetric  $E_v$  energy densities drop to an unacceptably low level. For example, with E/AM ratio >15  $\mu\text{L mg}^{-1}$ , the full-cell  $E_g$  could not be higher than 175  $\text{Wh kg}^{-1}$  even if reaching perfect sulfur utilization of 1,675  $\text{mAh g}^{-1}$  (Supplementary Fig. 1). Another key challenge, becoming increasingly known<sup>9,10</sup> to make Li-S batteries less interesting for important markets, is the low  $E_v$  that is a crucial factor for many applications. The  $E_v$  evaluated from

<sup>1</sup>Department of Nuclear Science and Engineering and Department of Materials Science and Engineering, Massachusetts Institute of Technology, Cambridge, MA, USA. <sup>2</sup>Beijing Advanced Innovation Center for Materials Genome Engineering, Key Laboratory for Renewable Energy, Beijing Key Laboratory for New Energy Materials and Devices, Beijing National Laboratory for Condensed Matter Physics, Institute of Physics, Chinese Academy of Sciences, Beijing, China. <sup>3</sup>Center of Materials Science and Optoelectronics Engineering, University of Chinese Academy of Sciences, Beijing, China. <sup>4</sup>Songshan Lake Materials Laboratory, Dongguan, Guangdong, China. <sup>5</sup>Department of Electrical Engineering and Computer Science, Massachusetts Institute of Technology, Cambridge, MA, USA. <sup>6</sup>Advanced Materials Lab, Samsung Advanced Institute of Technology America, Burlington, MA, USA. <sup>7</sup>Institute of New Energy for Vehicles, School of Materials Science and Engineering, Tongji University, Shanghai, China.

\*e-mail: [suoliumin@iphy.ac.cn](mailto:suoliumin@iphy.ac.cn); [liju@mit.edu](mailto:liju@mit.edu)

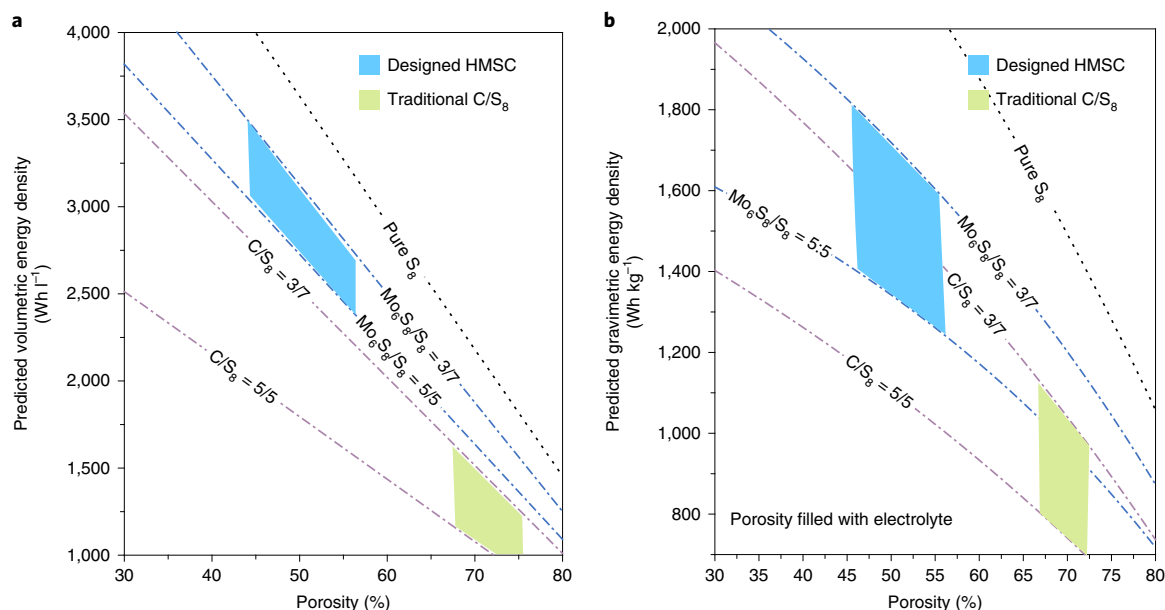


**Fig. 1 | Design strategy for jointly high gravimetric-volumetric energy density. a, b.** The relationship between cathode porosity and predicted cathode-specific  $e_v$  (**a**) and  $e_g$  (**b**) of the hybrid  $\text{Mo}_6\text{S}_8/\text{S}_8$  cathode with all carbon included (hereafter referred to as HMSC) and  $\text{C}/\text{S}_8$  cathode with different  $\text{C}/\text{S}_8$  and  $\text{Mo}_6\text{S}_8/\text{S}_8$  ratios. We correlate the required electrolyte amount to porosity by assuming that the electrolyte fills all the porosity in the cathode. Our intercalation-conversion strategy in principle would enable much higher  $e_g$  and  $e_v$  than conventional  $\text{C}/\text{S}_8$  cathodes by reducing the cathode porosity from ~70 to 55 vol%. The calculation process is shown in Supplementary Note 1.

most studies<sup>5</sup> may be only  $\sim 400 \text{ Wh l}^{-1}$ , lower than the conventional  $\text{LiFePO}_4/\text{graphite}$  battery ( $\sim 500 \text{ Wh l}^{-1}$ )<sup>11</sup>.

Great progress has been made on various structured sulfur cathodes to ameliorate the LiPS shuttling effect including sulfur-metal oxides or chalcogenide composites, for example,  $\text{SiO}_2$  (refs. <sup>12,13</sup>),  $\text{TiO}_2$  (refs. <sup>14,15</sup>),  $\text{MnO}_2$  (refs. <sup>16–18</sup>),  $\text{TiS}_2$  (refs. <sup>19,20</sup>) and  $\text{VS}_2$  (ref. <sup>21</sup>). However, to reach high full-cell  $E_g$  and  $E_v$ , which is much more meaningful for pushing Li-S batteries into commercial development<sup>22,23</sup>, Li-S batteries must work under rigorous conditions including high active material loading, lean electrolyte and low cathode porosity. Until now, however, few reports have been devoted to improving the joint  $E_g$ - $E_v$  energy densities by decreasing the inactive components in sulfur cathodes. Nazar's group<sup>4</sup> developed a compact sulfur cathode using an in situ cross-linked elastomeric binder and successfully achieved a very low E/AM ratio of  $3.5 \mu\text{l mg}^{-1}$ . A PEO-based polymer developed by Liu's group<sup>8</sup> acting as both  $\text{Li}^+$  conducting binder and LiPS reservoir can further decrease the E/AM ratio to  $3.3 \mu\text{l mg}^{-1}$ . Smart design of the electrolyte<sup>24</sup> and the pore structure of hosts<sup>25</sup> has been reported to improve the performances of Li-S batteries under lean electrolyte conditions. In addition, three-dimensional free-standing electrode architecture has also shown the potential of a compact electrode under low E/AM ratio conditions<sup>26–28</sup>. However, most of the reported sulfur cathodes cannot outperform the commercial LIB in terms of the joint  $E_g$ - $E_v$ . To surpass today's LIB, it is essential to greatly diminish the inactive components, but it has been extremely challenging to achieve both high  $E_g$  and  $E_v$  by reducing cathode porosity and E/AM ratio simultaneously while maintaining acceptable rate capability.

To overcome this challenge, our strategy is to design an intercalation-conversion hybrid cathode material by introducing electrochemically active Chevrel-phase  $\text{Mo}_6\text{S}_8$  with fast lithium intercalation reactions and high tap density to hybridize with  $\text{S}_8$  (the HMSC material, Fig. 2a). The electronically conducting and electrochemically active  $\text{Mo}_6\text{S}_8$  can effectively decrease the usage of high-surface-area carbons due to its extremely low electrical resistance ( $0.102 \Omega \text{ sq}^{-1}$  by a four-point probe method), reducing

cathode porosity from  $\sim 70$  to 55 vol%. Such a hybrid design would, in principle, enable much higher  $E_g$  and  $E_v$  than traditional  $\text{C}/\text{S}_8$  cathodes. The Chevrel-phase  $\text{Mo}_6\text{S}_8$  has several unique properties. First, unlike most previous inactive materials employed in cathodes<sup>13,14,29–39</sup>, it is able to contribute its own capacity in an ether-based electrolyte within the same voltage window as  $\text{S}_8$  (1.7–2.8 V):  $4\text{Li}^+ + 4e^- + \text{Mo}_6\text{S}_8 \leftrightarrow \text{Li}_4\text{Mo}_6\text{S}_8$ . Second, this reaction is intercalative, and therefore has fast kinetics since  $\text{Li}_x\text{Mo}_6\text{S}_8$  has a high polaron mobility ( $\text{Mo}^{2+} \leftrightarrow \text{Mo}^{3+}$ ). Third, because the theoretical density of  $\text{Mo}_6\text{S}_8$  ( $5.04 \text{ g cm}^{-3}$ ) is much higher than that of  $\text{S}_8$  ( $2.07 \text{ g cm}^{-3}$ ), the volumetric energy density of  $\text{Mo}_6\text{S}_8$  is actually very respectable,  $1,400 \text{ Wh l}^{-1}$ , with an intrinsic rate capability comparable to  $\text{LiFePO}_4$ . Fourth, the affinity for LiPS can be greatly enhanced via in situ electrochemical lithiation of  $\text{Mo}_6\text{S}_8$  to form  $\text{Li}_x\text{Mo}_6\text{S}_8$ , thereby suppressing the shuttling effect and resulting in stable cyclability. Fifth, we also find that the  $\text{Mo}_6\text{S}_8$  component improves the rheological properties of the slurry: the HMSC slurry has similar flow characteristics to the LIB slurry when coated on the current collector, it can be hard-pressed and is less prone to cracking, allowing us to easily reach high loadings such as  $6.2 \text{ mg cm}^{-2}$  for  $\text{S}_8$  and  $6.1 \text{ mg cm}^{-2}$  for  $\text{Mo}_6\text{S}_8$ . Sixth and finally, after drying, even with much reduced porosity, the electrolyte wets the cathode easily. The mechanically hard  $\text{Mo}_6\text{S}_8$  with fast  $\text{Li}^+$  transport and nearly zero volume change during charge-discharge, is an ideal backbone to immobilize soft sulfur species and unlock their high gravimetric capacity. This material combination of  $\text{Mo}_6\text{S}_8$  and  $\text{S}_8$  is akin to the relation between the primer and the TNT in explosives, with one igniting quickly and another having high gravimetric energy density.

We would also like to add that the HMSC containing only  $\sim 10 \text{ wt}\%$  carbon (similar to a typical LIB cathode) shows good rate capability to  $6 \text{ mA cm}^{-2}$  and stable long-term cycling performance. More importantly, the cathode porosity is tremendously reduced and an extremely low E/AM ratio of  $1.2 \mu\text{l mg}^{-1}$  can be realized. In particular, we can successfully make Ah-level pouch cells delivering high joint  $E_g$  and  $E_v$  of  $366 \text{ Wh kg}^{-1}$  and  $581 \text{ Wh l}^{-1}$ , outperforming both the Li-S and the commercial LIB in joint energy densities.

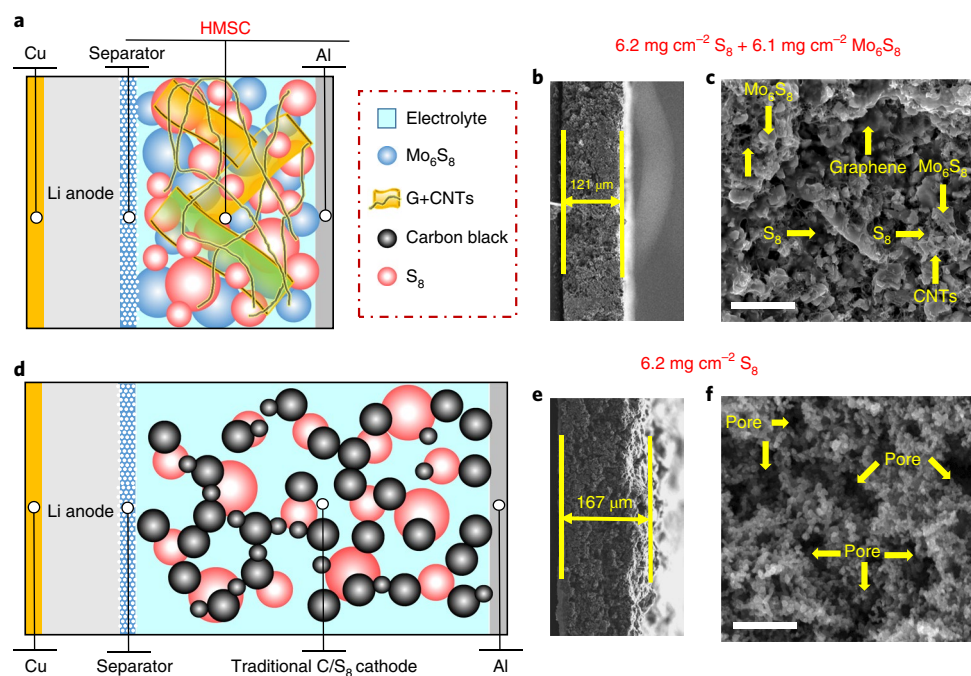
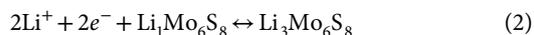


**Fig. 2 | Characterizations of the HMSC and traditional C/S<sub>8</sub> cathode.** **a–f**, Illustration of the Li–S batteries with our HMSC (**a–c**) and the C/S<sub>8</sub> cathode (**d–f**). SEM images show their cross-sections (**b,e**) and surfaces (**c,f**). The HMSC contains 6.2 mg cm<sup>-2</sup> S<sub>8</sub> and 6.1 mg cm<sup>-2</sup> Mo<sub>6</sub>S<sub>8</sub> while the C/S<sub>8</sub> cathode contains only 6.2 mg cm<sup>-2</sup> S<sub>8</sub>. Compared with the C/S<sub>8</sub> cathode, our HMSC has much lower electrode porosity and packing density. Scale bars, 1 μm.

### Fabrication and characterization of the HMSC cathode

Chevrel-phase Mo<sub>6</sub>S<sub>8</sub> is a unique class of compounds that can accommodate both multivalent and monovalent cations<sup>40</sup>. Due to its unique open and stable structure, the Mo<sub>6</sub>S<sub>8</sub> Chevrel phase features fast ion transport and good structural stability during lithiation/delithiation with a theoretical specific capacity of 128 mAh g<sup>-1</sup> (refs. <sup>41,42</sup>). Although Mo<sub>6</sub>S<sub>8</sub> has received attention as cathode/anode materials for Mg batteries<sup>43</sup> and aqueous Li-ion batteries<sup>41</sup>, it has not been applied in Li–S batteries. In the operating voltage window of Li–S batteries from 1.7 to 2.8 V, the stoichiometry of Li insertion into Mo<sub>6</sub>S<sub>8</sub> involves three stages<sup>40</sup>,



The cyclic voltammetry profile in Supplementary Fig. 2 shows three cathodic peaks and three anodic peaks corresponding to equations (1)–(3). The lack of obvious decay in peak intensities indicates excellent reversibility of Li<sub>x</sub>Mo<sub>6</sub>S<sub>8</sub> in the ether-based electrolyte. The scanning electron microscopy (SEM) micrograph in Supplementary Fig. 3a reveals the irregular-shaped particles ranging from several hundred nanometres to several micrometres. A representative high-resolution transmission electron microscopy (HRTEM) image in Supplementary Fig. 3b clearly shows lattice fringes with a spacing of 0.36 nm, corresponding to (003) plane of rhombohedral Mo<sub>6</sub>S<sub>8</sub>.

The synthesis procedure of the HMSC material is shown in Supplementary Fig. 4. Carbon nanotubes (CNTs), graphene and Mo<sub>6</sub>S<sub>8</sub> were firstly ball-milled to obtain a uniform mixture (Supplementary Fig. 5), and then a wet method<sup>15,18</sup> was used to deposit solid sulfur. The HMSC cathode contains 10 wt% carbonaceous materials (CNT/graphene), 85 wt% active S<sub>8</sub> + Mo<sub>6</sub>S<sub>8</sub> and

5 wt% binder. The X-ray diffraction (XRD) result (Supplementary Fig. 6) clearly indicates that the Mo<sub>6</sub>S<sub>8</sub> and S<sub>8</sub> are the dominant components of HMSC. The SEM image in Fig. 2c reveals a dense and uniform cathode morphology where CNTs and graphene can support a good three-dimensionally interconnected conductive network. Due to its good electronic conductivity and high tap density, the uniformly dispersed Mo<sub>6</sub>S<sub>8</sub> not only offers an electronic matrix as good as carbon but also greatly decreases the carbon content from ~30 wt% in traditional C/S<sub>8</sub> cathodes to ~10 wt%, as low as traditional LIB cathodes. In contrast, the C/S<sub>8</sub> cathode shows a very porous morphology due to the large carbon content (36 wt%, Fig. 2f). The replacement of low-tap-density inactive components by high-tap-density electrochemically active components brings in significant advantages, described as follows.

The packing density of active materials can be effectively increased (Fig. 2a,b). The electrode thickness with 6.2 mg cm<sup>-2</sup> S<sub>8</sub> for the C/S<sub>8</sub> cathode is 167 μm (Fig. 2e). In contrast, our HMSC with 6.2 mg cm<sup>-2</sup> S<sub>8</sub> plus another 6.1 mg cm<sup>-2</sup> Mo<sub>6</sub>S<sub>8</sub> is only 121 μm (Fig. 2b). According to the normalized electrode thickness per 1 mg cm<sup>-2</sup> S<sub>8</sub> summarized from previous studies in Supplementary Fig. 7, the typical values in most plausible C/S<sub>8</sub> electrodes are below 500 g l<sup>-1</sup> (only S<sub>8</sub>). However, the overall packing density of active materials in the HMSC doubles to 1,047 g l<sup>-1</sup>, including 526 g l<sup>-1</sup> (S<sub>8</sub>) plus 521 g l<sup>-1</sup> (Mo<sub>6</sub>S<sub>8</sub>).

Furthermore, it is much easier for our HMSC to obtain crack-free electrodes with high sulfur loading, which is essential for practically viable batteries<sup>44</sup> than traditional C/S<sub>8</sub> cathodes. For C/S<sub>8</sub> cathodes with high fraction of carbonaceous materials to achieve successful casting, the slurry needs many solvents to be diluted to a proper viscosity. Large cracks and morphology inhomogeneities in the C/S<sub>8</sub> cathode are observed due to excessive shrinkage during drying, while the HMSC is smooth and free of cracks (Supplementary Fig. 8). Benefiting from this approach, we can obtain a crack-free and highly compact electrode with very high loading of active materials (as high as 10 mg cm<sup>-2</sup> S<sub>8</sub> and 9.9 mg cm<sup>-2</sup> Mo<sub>6</sub>S<sub>8</sub>, Supplementary Fig. 9). When coated on current collector, the slurry mechanically

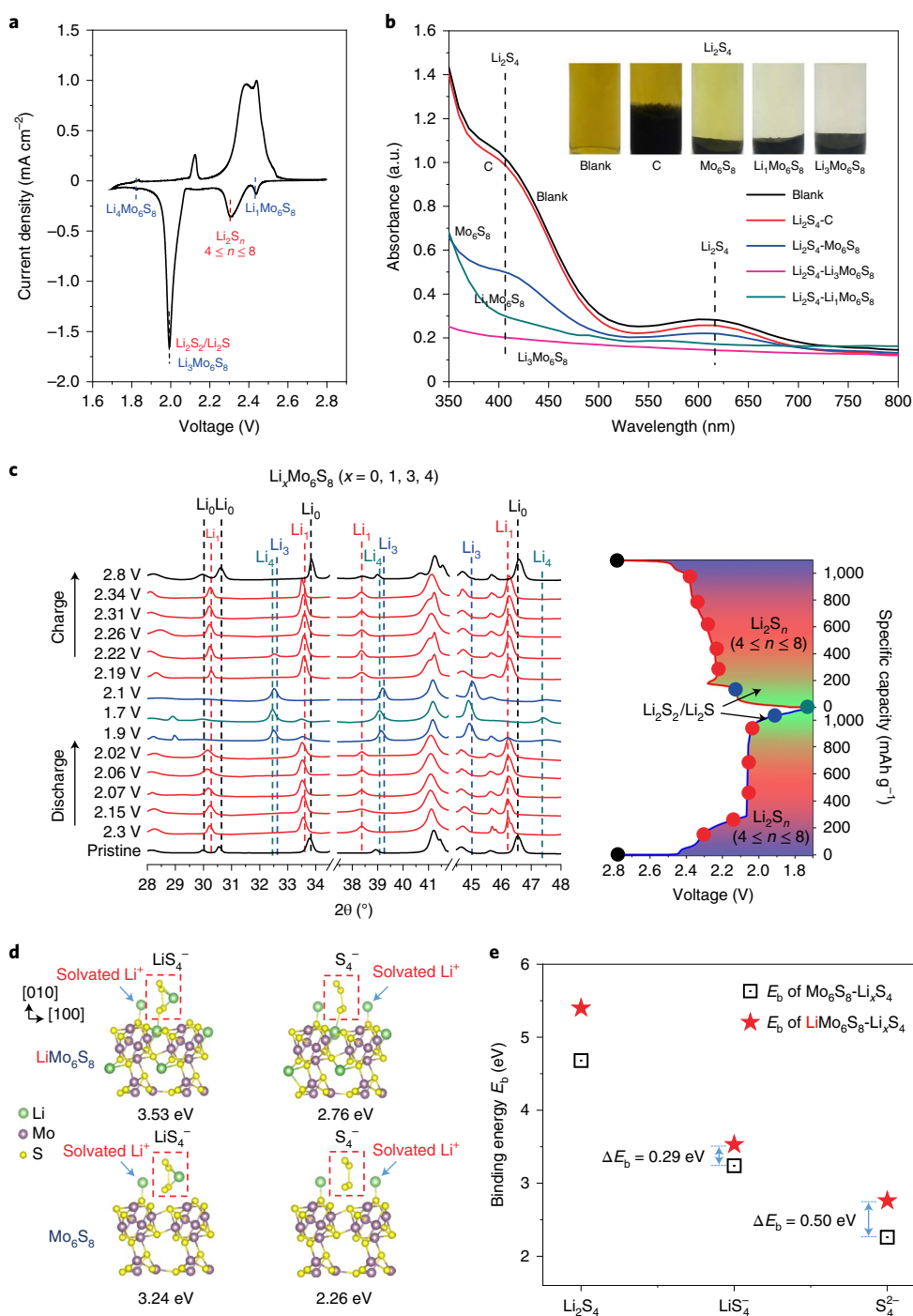


**Fig. 3 | Investigation of the interaction between Li<sub>x</sub>Mo<sub>6</sub>S<sub>8</sub> and LiPS. **a**, Cyclic voltammogram plot of a Li|HMSC cell. **b**, Visual discrimination (inset) and ultraviolet-visible spectra of the Li<sub>2</sub>S<sub>4</sub> solutions after exposure to C, Mo<sub>6</sub>S<sub>8</sub>, Li<sub>1</sub>Mo<sub>6</sub>S<sub>8</sub>, Li<sub>3</sub>Mo<sub>6</sub>S<sub>8</sub> and Li<sub>4</sub>Mo<sub>6</sub>S<sub>8</sub>. **c**, In situ XRD measurements of a Li|HMSC cell. **d**, Relaxed structures of LiS<sub>4</sub><sup>-</sup> and S<sub>4</sub><sup>2-</sup> after the respective step-wise ionization on their absorption on the Mo<sub>6</sub>S<sub>8</sub> (100) and LiMo<sub>6</sub>S<sub>8</sub> (100) surfaces, determined from density functional theory calculations. **e**, Comparison of different binding energies (E<sub>b</sub>) between LiPS and Mo<sub>6</sub>S<sub>8</sub>/LiMo<sub>6</sub>S<sub>8</sub> before and after the step-wise ionization.**

feels like traditional LIB cathode slurry, and not like the typical C/S<sub>8</sub> slurry, due to the presence of hard Mo<sub>6</sub>S<sub>8</sub> articles as dispersants. It can be hard-pressed like a LIB cathode, unlike a typical C/S<sub>8</sub> cathode.

### Enhanced interaction between Li<sub>x</sub>Mo<sub>6</sub>S<sub>8</sub> and LiPS

Unlike conventional inactive host materials with a fixed affinity for LiPS, the chemical composition of Li<sub>x</sub>Mo<sub>6</sub>S<sub>8</sub> undergoes continuous variation during the charge-discharge processes, thus presenting a different chemical adsorption to LiPS with the voltage change. The

cyclic voltammogram characteristics measured on an HMSC|PP|Li half-cell in Fig. 3a clearly point to multiple redox reactions during the charge-discharge process and the highly reversible nature of the electrode. The representative cathodic peak at 2.43 V can be attributed to the lithiation of Mo<sub>6</sub>S<sub>8</sub> to Li<sub>1</sub>Mo<sub>6</sub>S<sub>8</sub>. The two representative cathodic peaks at roughly 2.3 and 2.0 V are attributed to the lithiation of S<sub>8</sub> to soluble LiPS (Li<sub>2</sub>S<sub>n</sub>, 4 ≤ n ≤ 8) and insoluble short-chain Li<sub>2</sub>S<sub>2</sub>/Li<sub>2</sub>S, respectively. The unrecognized cathodic peaks of Li<sub>3</sub>Mo<sub>6</sub>S<sub>8</sub> and Li<sub>4</sub>Mo<sub>6</sub>S<sub>8</sub> may result from the overlap with redox

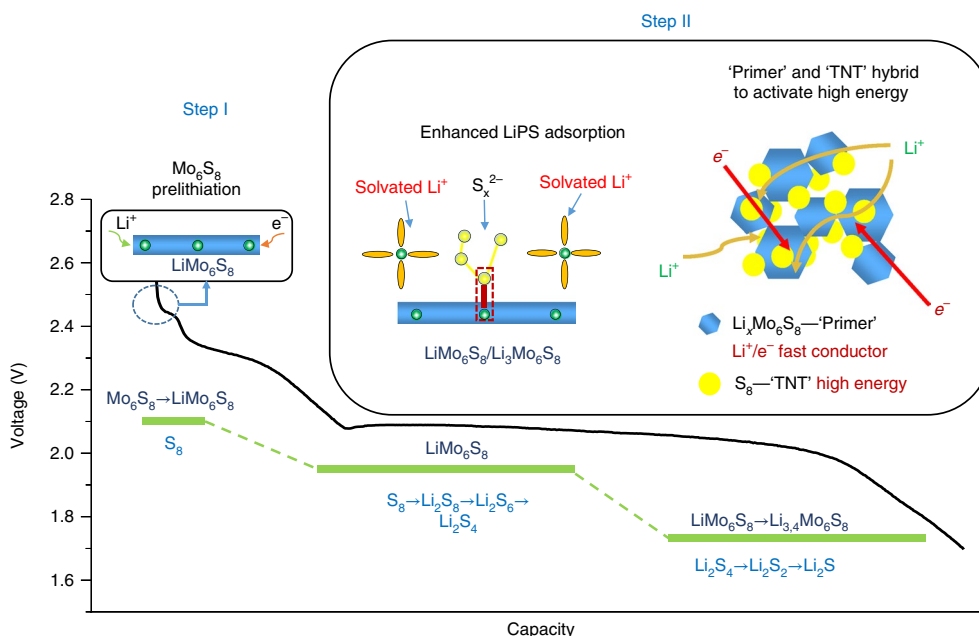


**Fig. 4 | The roles of the Chevrel-phase  $\text{Mo}_6\text{S}_8$  in the HMSC.** Step I is a pre-lithiation step, proceeding before the reduction of sulfur ( $>2.4$  V). Step II is the post-lithiation step, in which the lithiated  $\text{Mo}_6\text{S}_8$  induces two functions. First, the interaction between LiPS and  $\text{LiMo}_6\text{S}_8/\text{Li}_3\text{Mo}_6\text{S}_8$  is enhanced by the formation of the bonding between Li and S that dominates the adsorptive interaction. Second, the intercalative reaction in  $\text{Li}_x\text{Mo}_6\text{S}_8$  provides a fast Li-ion transport channel that can unlock the gravimetric capacity of  $\text{S}_8$ .

peaks of  $\text{S}_8$ . To gain an insight into the phase evolution of  $\text{Li}_x\text{Mo}_6\text{S}_8$ , we conducted in situ XRD analysis during the charge-discharge process (Fig. 3c). In the initial stage, the pristine sample contains only rhombohedral  $\text{Mo}_6\text{S}_8$ . It is noted that no obvious peak associated with  $\text{S}_8$  can be identified because of its much lower intensity compared to  $\text{Mo}_6\text{S}_8$ . When the cell is initially discharged to 2.3 V, three characteristic peaks located at  $30.7$ ,  $33.9$  and  $46.7^\circ$  shift towards lower angles indicating an increase in the lattice constants after Li intercalation, corresponding to rhombohedral  $\text{Li}_1\text{Mo}_6\text{S}_8$  (JCPDS: 081–0858). Discharging further from 2.3 to 2.0 V, rhombohedral  $\text{Li}_1\text{Mo}_6\text{S}_8$  is the dominant phase accompanying the continuous reduction of  $\text{S}_8$  to soluble high-order LiPS ( $\text{Li}_2\text{S}_n$ ,  $4 \leq n \leq 8$ ) and partially insoluble low-order  $\text{Li}_2\text{S}_2/\text{Li}_2\text{S}$ . When the cell is further discharged to 1.9 and 1.7 V, the characteristic peaks continue to shift to lower angles indicating the emergence of  $\text{Li}_3\text{Mo}_6\text{S}_8$  (JCPDS: 81–0859) and  $\text{Li}_4\text{Mo}_6\text{S}_8$  (JCPDS: 81–0860) corresponding to the full conversion from LiPS to solid  $\text{Li}_2\text{S}$ . During charging, all the phase evolution is reversible.

These results reveal that the transition from  $\text{S}_8$  to LiPS occurs along with the transformation of  $\text{Li}_1\text{Mo}_6\text{S}_8$  to  $\text{Li}_3\text{Mo}_6\text{S}_8$ , suggesting that the  $\text{Li}_1\text{Mo}_6\text{S}_8/\text{Li}_3\text{Mo}_6\text{S}_8$  dominates the adsorption of LiPS. To further observe such interactions, the polysulfide adsorption experiment (Fig. 3b, inset) is designed by the visual discrimination of the colour changes of the  $\text{Li}_2\text{S}_4$  solution with the same amount of adsorbent materials (C,  $\text{Mo}_6\text{S}_8$ ,  $\text{Li}_1\text{Mo}_6\text{S}_8$ ,  $\text{Li}_3\text{Mo}_6\text{S}_8$ ). The intrinsic ability of  $\text{Mo}_6\text{S}_8$  to adsorb  $\text{Li}_2\text{S}_4$  reveals the strong interaction between metal sulfide surface and LiPS<sup>1,35</sup>, whereas the carbon- $\text{Li}_2\text{S}_4$  solution remains almost the same as the blank  $\text{Li}_2\text{S}_4$ , indicative of weak surface interaction (and consequently unimpressive electrocatalytic activity). However, it is intriguing to note that the  $\text{Li}_1\text{Mo}_6\text{S}_8$  and  $\text{Li}_3\text{Mo}_6\text{S}_8$  show almost transparent solutions after exposure to LiPS. Such strong adsorption capability can be further verified by ex situ ultraviolet-visible spectroscopy measurements. Figure 3b clearly demonstrates the much higher absorbance of  $\text{Li}_1\text{Mo}_6\text{S}_8$ - $\text{Li}_2\text{S}_4$  and  $\text{Li}_3\text{Mo}_6\text{S}_8$ - $\text{Li}_2\text{S}_4$  solutions than  $\text{Mo}_6\text{S}_8$ - $\text{Li}_2\text{S}_4$  in the characteristic adsorption regions of  $\text{Li}_2\text{S}_4$  at  $\sim 410$  and  $615$  nm<sup>45</sup>. Furthermore, the well-matched S and Mo distribution in the cycled HMSC

(Supplementary Fig. 10) further indicates the excellent adsorption capability of  $\text{Li}_x\text{Mo}_6\text{S}_8$  with LiPS.

To address the fundamental mechanism of such enhanced affinity for LiPS, first-principles calculations were performed. Most of the previous modelling studies constructed oversimplified molecule-on-slab adsorption configurations. Without taking the LiPS dissolution in electrolyte into account, it would probably result in overestimating the binding energies. In fact, the solvation plays a very important role of triggering the ionization of LiPS into solvated  $\text{Li}^+$  (electrolyte) cations and  $\text{S}_n^{2-}$  (electrolyte) anion (Fig. 3d). Therefore, the actual structure of LiPS in electrolytes could be  $\text{LiS}_n^-/\text{S}_n^{2-}$  and solvated  $\text{Li}^+$ . Herein,  $\text{Li}_2\text{S}_4$  is employed as the representative LiPS. Figure 3d illustrates the adsorption configurations for  $\text{Li}_2\text{S}_4^-$  and  $\text{S}_4^{2-}$  on  $\text{Mo}_6\text{S}_8$  and  $\text{LiMo}_6\text{S}_8$  surfaces, respectively. The adsorptive interaction is dominated by the bonding between Li and S. Therefore, during the step-wise ionization of  $\text{Li}_2\text{S}_4$  its binding strength with the substrate tends to drop with fewer Li atoms in  $\text{Li}_2\text{S}_4^-$ . However, compared to pristine  $\text{Mo}_6\text{S}_8$ , the  $\text{LiMo}_6\text{S}_8$  with additional bond demonstrates a better anchoring capability that is reflected not only by the higher binding energy but also the smaller decrease in binding energy during the step-wise ionization (Fig. 3e). In the ether-based electrolyte, the interaction between the Li cation and polysulfide anion weakens with the increase of polysulfide chain length<sup>46</sup> and, consequently, there is an obvious decrement in the anchoring capability of the substrates, especially for those mainly via polar-polar Li-S interaction<sup>7</sup>. We propose from the simulation results that the prelithiated substrate has the advantage of stronger LiPS adsorption capability over the unlithiated one in the real LiPS-electrolyte system via the additional Li-S binding.

We propose a two-step role of Chevrel-phase  $\text{Mo}_6\text{S}_8$  in Fig. 4. Step I is the pre-lithiation step ( $>2.4$  V). During this step,  $\text{Mo}_6\text{S}_8$  is transformed to  $\text{Li}_x\text{Mo}_6\text{S}_8$  ( $x=1$ ) before the reduction of sulfur. Subsequently, the  $\text{Li}_x\text{Mo}_6\text{S}_8$  exhibits two unique functions in Step II—the post-lithiation step. One is the enhanced LiPS adsorption: long-chain LiPS forms in the presence of  $\text{LiMo}_6\text{S}_8$ , benefiting the suppression of the shuttling effect and thus improving the cycling stability. Another is that the intercalative reaction in  $\text{Li}_x\text{Mo}_6\text{S}_8$

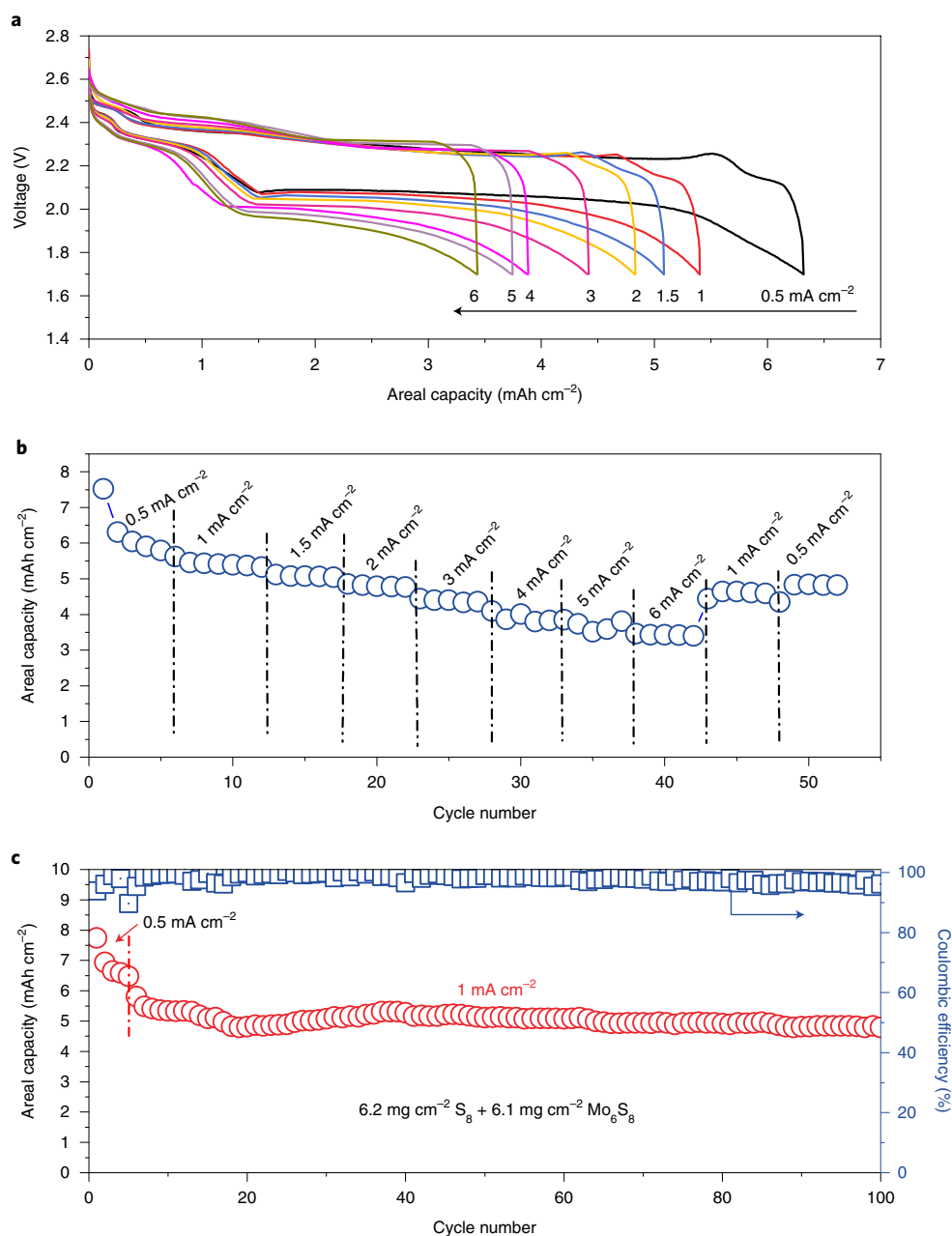


**Fig. 5 | Electrochemical performance of the Li|HMSC coin cell.** In this coin cell, we use:  $6.2 \text{ mg cm}^{-2} \text{ S}_8$ ,  $6.1 \text{ mg cm}^{-2} \text{ Mo}_6\text{S}_8$  and an E/AM ratio of  $2.4 \mu\text{g mg}^{-1}$ . **a, b.** The charge-discharge profiles (**a**) and rate capability (**b**) at various current densities from  $0.5 \text{ mA cm}^{-2}$  to  $6 \text{ mA cm}^{-2}$ . **c.** Cycling life and Coulombic efficiency at  $1 \text{ mA cm}^{-2}$ .

could provide a fast  $\text{Li}^+$  transporting channel, which is critical for unlocking the high gravimetric capacity of  $\text{S}_8$ .

### Electrochemical performances

Despite the attractive high theoretical energy densities of a Li-S battery, it becomes increasingly clear that to achieve high full-cell  $E_g$  or  $E_v$ , improving the capacity at high sulfur loadings and keeping decent rate capability while decreasing the E/AM ratio and cathode porosity, is tremendously challenging<sup>26,28,44,47</sup>. To reach an  $E_g$  value roughly equal to  $400 \text{ Wh kg}^{-1}$  or higher, it was suggested<sup>48,49</sup> that the E/AM ratio should be below  $3 \mu\text{g mg}^{-1}$  or even  $1.9 \mu\text{g mg}^{-1}$ , and the cathode porosity must also be reduced as much as possible to achieve high  $E_v$ <sup>5</sup>. However, for standard C/ $\text{S}_8$  cathodes, both high E/AM ratio and cathode porosity are required due to kinetics requirements.

The role of E/AM in attaining good electrochemical performance for C/ $\text{S}_8$  is shown in Supplementary Fig. 11. At E/AM =  $6 \mu\text{g mg}^{-1}$ , the areal capacity of the C/ $\text{S}_8$  cathode reached about  $5 \text{ mAh cm}^{-2}$  at  $1 \text{ mA cm}^{-2}$ , which dropped to  $<1 \text{ mAh cm}^{-2}$  at  $1 \text{ mA cm}^{-2}$  after decreasing the E/AM ratio to  $5 \mu\text{g mg}^{-1}$  due to the increased cell impedance<sup>26</sup>. The required E/AM ratio can be effectively reduced to  $4 \mu\text{g mg}^{-1}$  by introducing only 20 wt%  $\text{Mo}_6\text{S}_8$  into the cathode (Supplementary Fig. 12). By using an equal weight fraction of  $\text{Mo}_6\text{S}_8$  and  $\text{S}_8$  (Supplementary Fig. 13) with only ~10 wt% carbon in the cathode, the E/AM ratio can be successfully reduced to  $2.4 \mu\text{g mg}^{-1}$ . The voltage profiles in Fig. 5a show long and flat discharge plateaus at  $\sim 2.1 \text{ V}$  and low overpotential even at high current densities, indicating good electronic/ionic conductivities in the HMSC. In addition, apparent charge-discharge plateaus from  $\text{Mo}_6\text{S}_8 \leftrightarrow \text{Li}_1\text{Mo}_6\text{S}_8$

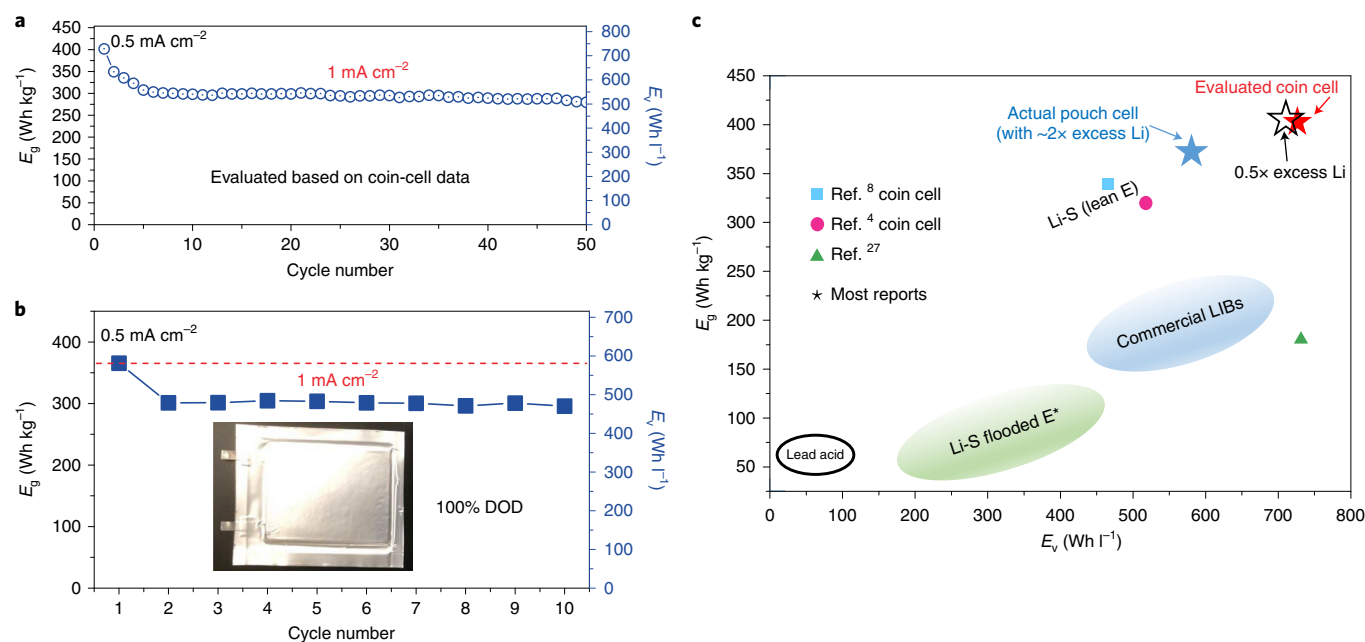


**Fig. 6 | The  $E_g$  and  $E_v$  of the Li|HMSC cell.** **a**, The coin-cell configuration constructed by the HMSC cathode ( $6.9 \text{ mg cm}^{-2} \text{ S}_8 + 6.8 \text{ mg cm}^{-2} \text{ Mo}_6\text{S}_8$ ) with an E/AM ratio  $\sim 1.5 \mu\text{l mg}^{-1}$  on cycling. **b**, The pouch-cell configuration constructed by the HMSC cathode with E/AM ratio  $\sim 1.2 \mu\text{l mg}^{-1}$  and  $\sim 2\times$  Li excess ( $100 \mu\text{m}$  for one side). DOD, depth of discharge. **c**, The comparison of projected full-cell energy densities based on our data and representative publications. Reference <sup>27</sup> is evaluated on the basis of their pouch-cell data, and other references are based on coin-cell data.

at  $\sim 2.4 \text{ V}$  can also be observed from Fig. 5a, further verifying that  $\text{Mo}_6\text{S}_8$  indeed works with  $\text{S}_8$  together as a secondary active material contributing an extra  $\sim 10\%$  capacity (Supplementary Fig. 14). Our HMSC cathode exhibited excellent rate capability (Fig. 5b), achieving 7.5, 4.9, 4.0 and  $3.5 \text{ mAh cm}^{-2}$  at current densities of 0.5, 2, 4 and  $6 \text{ mA cm}^{-2}$ , respectively. The long-term cycling performance in Fig. 5c showed a high initial capacity of  $7.8 \text{ mAh cm}^{-2}$  with a good capacity retention of 83% over 100 cycles. Such good cycling stability could be attributed to the favourable LiPS adsorption capability of  $\text{Li}_x\text{Mo}_6\text{S}_8$ . In contrast, severe shuttling behaviour was found for the C/ $\text{S}_8$  cathode without  $\text{Mo}_6\text{S}_8$  (Supplementary Fig. 15). For such a high loading electrode and low E/AM, the rate capability and cycling stability are impressive.

Electrochemical impedance spectroscopy was conducted on HMSC cathode before and after cycling (Supplementary Fig. 16). The equivalent electrical circuit  $R_0$  corresponded to the Ohmic resistance from the electrolyte solution.  $R_1/\text{CPE}_1$  from the first semi-circle in the high-frequency range was assigned to the resistance of the surface layers on both cathode and anode.  $R_2/\text{CPE}_2$  from the second semi-circle in the low-frequency range was attributed to the charge transfer process occurring at the interface between the cathode and electrolyte.  $R_0$ ,  $R_1$  and  $R_2$  remained low and stable (Supplementary Fig. 17), indicating a favourable and well-maintained conducting network during cycling. The galvanostatic intermittent titration technique was also conducted to evaluate the state of health of the Li|HMSC battery after 100 cycles (Supplementary Fig. 18). In the voltage region between 2.1 and 2.5 V, small voltage changes on removing the current indicated relatively fast kinetics. Both the quasi-equilibrium potentials and the discharge plateau in the lower voltage region between 1.7 and 2.1 V remained stable and flat, suggesting a good state of health after 100 cycles. This is encouraging, since the cycle life of the Li|HMSC battery is not just controlled by the cathode, but also controlled by the Li metal anode that depletes the electrolyte<sup>4</sup> (Supplementary Fig. 19), which becomes more challenging under such lean electrolyte conditions.

For comparison of the full-cell energy densities of different Li-S works, we used a simplified pouch-cell model (Supplementary Fig. 20) to evaluate the coin-cell data, with  $2\times$  excess Li metal anode, cathode, electrolyte, Al current collector and separator all included. Our Li|HMSC cell with an E/AM ratio of  $\sim 1.5 \mu\text{l mg}^{-1}$  and low cathode porosity brought out extremely high joint  $E_g$  and  $E_v$  of  $402 \text{ Wh kg}^{-1}$  and  $731 \text{ Wh l}^{-1}$ , respectively, at  $0.5 \text{ mA cm}^{-2}$  and good cycling stability (Fig. 6a). The  $E_g$  is much higher than the commercial LIBs and the  $E_v$  is comparable to commercial LIBs. To the best of our knowledge, our full-cell joint  $E_g$ - $E_v$  represents a very high level compared with most Li-S studies (Fig. 6c).

To validate the calculations above, 1 Ah-level pouch cells with multilayer cathodes (HMSC) and anodes ( $\sim 2\times$  excess Li metal<sup>20</sup>, that is,  $15\text{-}\mu\text{m}$ -thick Li metal opposite to every  $1 \text{ mAh cm}^{-2}$  HMSC), were assembled (Supplementary Fig. 21). The Li|HMSC pouch cell delivered energy densities of  $366 \text{ Wh kg}^{-1}$  and  $581 \text{ Wh l}^{-1}$  (Fig. 6b), comparable to our projected coin-cell data. The cycling of the Li|HMSC pouch cell was very stable. The voltage profiles (Supplementary Fig. 22) were identical to those of coin cells. The E/AM ratio in the pouch cell can be further reduced to a very lean electrolyte condition of  $1.2 \mu\text{l mg}^{-1}$ , under which the pouch cell with traditional C/ $\text{S}_8$  cathodes cannot even work (Supplementary Fig. 23). It is worth pointing out that there is still much room to further enhance the joint energy densities by optimizing both the mass-production process and other mechanical parameters for making the pouch cell, which is well-known to influence the practical performance<sup>8</sup>. For example, if  $0.5\times$  excess Li is used, we can further boost the energy densities to  $405 \text{ Wh kg}^{-1}$  and  $712 \text{ Wh l}^{-1}$  (Fig. 6c).

## Conclusion

An intercalation-conversion composite cathode, created by hybridizing a mechanically hard Chevrel-phase  $\text{Mo}_6\text{S}_8$  with fast lithium intercalation reactions and the mechanically soft  $\text{S}_8$  with high gravimetric energy density, is reported in this paper. It has been shown to be an effective way to decrease the inactive components in Li-S battery cathodes, thus simultaneously achieving high  $E_g$ - $E_v$

and good rate capability. The  $\text{Mo}_6\text{S}_8$  is an ideal backbone to immobilize soft sulfur species and unlock their high gravimetric capacity. The excellent areal capacity and cyclability at high active material loadings were enabled under realistic but challenging conditions including very low carbon content ( $\sim 10$  wt%), cathode porosity ( $\sim 55$  vol%) and E/AM ratio ( $1.2 \mu\text{L mg}^{-1}$ ). To further demonstrate the practicality of our approach, we built Ah-level Li|HMSC pouch cells, which displayed very high joint energy densities of  $366 \text{ Wh kg}^{-1}$  and  $581 \text{ Wh l}^{-1}$  with quite abundant  $2\times$  excess lithium metal. This work overcomes the major limitations associated with pure anion-redox materials and will open new avenues for developing simultaneously high gravimetric and volumetric energy density batteries.

## Methods

**Preparation of  $\text{Mo}_6\text{S}_8$ .** Chevrel-phase  $\text{Mo}_6\text{S}_8$  was fabricated by a solid-state synthesis method. First,  $\text{CuS}$  (99% Sigma-Aldrich),  $\text{Mo}$  (99.99% Sigma-Aldrich) and  $\text{MoS}_2$  (99% Sigma-Aldrich) were ground for 0.5 h, then the mixtures were pressed into a pellet by a 14-mm-diameter mould and sealed in Swagelok stainless steel tube, which was gradually heated to  $900^\circ\text{C}$  for 24 h at  $2^\circ\text{C min}^{-1}$  in argon. Subsequently, the as-received  $\text{Cu}_2\text{Mo}_6\text{S}_8$  precursors were added into a 6 M HCl solution for 12 h with oxygen bubbling to leach out Cu. After the reaction, the obtained  $\text{Mo}_6\text{S}_8$  powder was centrifuged and washed with deionized water three times followed by drying at  $60^\circ\text{C}$  overnight under a vacuum.

**Preparation of the HMSC material.** Sulfur was synthesized by a wet-method on the basis of the reaction between  $\text{Na}_2\text{S}_2\text{O}_3$  and  $\text{H}_2\text{SO}_4$ . First, CNTs, graphene (both from Dr Bunshi Fugetsu, The University of Tokyo) and  $\text{Mo}_6\text{S}_8$  were ball-milled to obtain a uniform slurry into which  $\text{Na}_2\text{S}_2\text{O}_3$  was dissolved. Subsequently, 0.5 M  $\text{H}_2\text{SO}_4$  was slowly added into the CNTs/graphene/ $\text{Mo}_6\text{S}_8$ / $\text{Na}_2\text{S}_2\text{O}_3$  mixture and stirred at room temperature for 2 h. The HMSC material was obtained after the mixture was washed, centrifuged and then dried at  $60^\circ\text{C}$  overnight.

**LiPS adsorption study.**  $\text{Mo}_6\text{S}_8$  powders were pressed into 14-mm-diameter pellets. Then, CR2032-type coin cells were then assembled using  $\text{Mo}_6\text{S}_8$  pellets as cathodes, Celgard separators and Li metal as anodes in the Ar-filled glove box. The electrolyte was 1 M lithium bis-(trifluoromethanesulfonyl) imide (LiTFSI) in a 1,3-dioxolane (DOL)-dimethoxyethane (DME) mixture (1:1, v/v) with 2 wt%  $\text{LiNO}_3$ . The cells were galvanostatically discharged to 2.3 and 1.9 V at a current density of  $0.2 \text{ mA cm}^{-2}$  using a Landt CT 2001A battery cycler to obtain electrochemical lithiated  $\text{Li}_1\text{Mo}_6\text{S}_8$  and  $\text{Li}_3\text{Mo}_6\text{S}_8$ , respectively. Finally, the  $\text{Li}_1\text{Mo}_6\text{S}_8$  and  $\text{Li}_3\text{Mo}_6\text{S}_8$  products were collected by washing and drying the cathode materials after disassembling the coin cells in the glove box.

$\text{Li}_2\text{S}_4$  solutions were synthesized by reacting lithium sulfide ( $\text{Li}_2\text{S}$ ) and elemental sulfur in the desired ratio in anhydrous DME solvent in an Ar-filled glove box. For the LiPS adsorption study,  $\text{Mo}_6\text{S}_8$ ,  $\text{Li}_1\text{Mo}_6\text{S}_8$ ,  $\text{Li}_3\text{Mo}_6\text{S}_8$  were added to glass vials. Subsequently,  $\text{Li}_2\text{S}_4$  solutions were added. Two blank vials were also filled with the same blank  $\text{Li}_2\text{S}_4$  solution and the  $\text{Li}_2\text{S}_4$ -carbon black (Timical, Super C65) mixture as control samples, respectively. The adsorption ability of  $\text{Mo}_6\text{S}_8$ ,  $\text{Li}_1\text{Mo}_6\text{S}_8$ ,  $\text{Li}_3\text{Mo}_6\text{S}_8$  and carbon on LiPS was qualitatively determined by using a ultraviolet-visible spectrometer (Perkin Elmer Lambda 1050 Spectrophotometer).

**Characterization.** The morphologies and microstructures were characterized by SEM (Zeiss Merlin high-resolution SEM) with energy-dispersive X-ray analysis and transmission electron microscopy (TEM, JOEL 2010F). The sulfur content was determined by thermogravimetric analyses (TG-DSC, SDT Q600) under nitrogen protection. In situ XRD was performed using a Rigaku Smartlab XRD system coupled with a specialized battery cell to monitor the phase evolution during the discharge and charge. The electronic conductivities were measured by a standard four-point-probe resistivity measurement system.

**Electrochemical measurements.** A slurry was fabricated by mixing 95 wt% of the HMSC and 2.5 wt% of styrene butadiene rubber aqueous binder, and 2.5 wt% of carboxymethyl cellulose binder. The obtained slurry was doctor-bladed onto a carbon-coated aluminum foil and then dried at  $60^\circ\text{C}$  for 12 h. Finally, all the electrodes were rolled and cut into round discs. CR2032-type coin cells were assembled using the HMSC cathode and Li metal anode in the Ar-filled glove box. The electrolyte was 0.6 M LiTFSI in a DOL-DME mixture (1:1, v/v) with 0.4 M  $\text{LiNO}_3$ . E/AM ratio is calculated by the electrolyte volume over the active materials mass (in our case,  $\text{Mo}_6\text{S}_8$  and  $\text{S}_8$  are both considered active materials). For E/AM ratio of  $1.5 \mu\text{L mg}^{-1}$ , Li metal was immersed into electrolyte for 12 h to form a passivation solid-electrolyte interphase layer before use. The cycling performances of the cells were measured by galvanostatic charge and discharge within the voltage window of 1.7–2.8 V versus  $\text{Li/Li}^+$  at various current densities using a Landt CT 2001A battery cycler. Cyclic voltammetry and electrochemical impedance spectroscopy measurements were taken using an electrochemical workstation (Gamry Instruments, Reference 3000). The galvanostatic intermittent titration

technique was conducted on the cycled batteries that were subjected to current pulse intervals with a current density of  $0.25 \text{ mA cm}^{-2}$  for 10 min, followed by 10 min rests until complete discharge.

**The evaluation of energy densities.** On the basis of the simplified pouch-cell configuration shown in Supplementary Fig. 20, the jellyroll  $E_g$  and  $E_v$  can be evaluated the basis of coin-cell data using the equations

$$E_g = \frac{VC}{\sum m_i} \quad (4)$$

$$E_v = \frac{VC}{\sum T_i} \quad (5)$$

where  $E_g$  and  $E_v$  are the full-cell gravimetric ( $\text{Wh kg}^{-1}$ ) and volumetric ( $\text{Wh l}^{-1}$ ) energy densities, respectively,  $V$  is the average output voltage (2.1 V is assumed),  $C$  is the areal capacity ( $\text{mAh cm}^{-2}$ ),  $m_i$  and  $T_i$  are the mass per unit square ( $\text{mg cm}^{-2}$ ) and the thickness (cm) of cell components including the cathode, anode ( $2\times$  Li excess is assumed), current collectors ( $\rho_{\text{Al}} \approx 2.7 \text{ g cm}^{-3}$ ), separator ( $\rho \approx 0.95 \text{ g cm}^{-3}$ ) and electrolyte ( $\rho \approx 1.2 \text{ g cm}^{-3}$ ). We do not take into account the electrolyte volume when calculating  $E_v$ . The jellyroll energy densities of pouch cells are calculated on the basis of actual measurements.

**Pouch-cell assembly.** First, the well-mixed slurry was double-side coated on carbon-coated Al foil and then dried at  $60^\circ\text{C}$  for 4 h. Second,  $4.3 \times 5.6 \text{ cm}^2$  electrodes were cut by a gas driven die cutter (MTI Corporation) and the electrode materials were carefully removed from tab areas to expose the Al foil. The assembly process of a pouch cell is as follows. First, the Ni tab was pressed to attach with the Li foil and then was covered with  $25\text{-}\mu\text{m}$ -thick Celgard separator. Second, the cathode and anode were carefully stacked layer-by-layer by hand to make a jellyroll cell. Third, the Al tab was welded together with cathodes. Finally, the jellyroll cell was vacuum-sealed by Al laminated films after injecting electrolyte.

**First-principles calculations.** We used the Perdew–Burke–Ernzerhof<sup>61</sup> exchange-correlational functional and the projector-augmented wave method<sup>62</sup> in our density functional theory (DFT) simulations implemented by the Vienna Ab Initio Simulation Package<sup>63</sup>. The DFT–Tkatchenko–Scheffler method<sup>64</sup> was used to take into account the van der Waals interactions in any adsorption processes. A plane wave basis set with an energy cutoff of 500 eV was adopted to expand the electronic wavefunctions. The Brillouin zone integration was conducted on a  $5 \times 5 \times 1$  Monkhorst–Pack  $k$ -point mesh. Atomic coordinates in all structures were relaxed until the maximum residual force was below  $0.02 \text{ eV \AA}^{-1}$ .

The  $\text{Mo}_6\text{S}_8$  (001) surface has the lowest energy ( $24 \text{ meV \AA}^{-2}$ ) and has been determined as the most stable surface among other low Miller index planes<sup>65</sup>. A slab of 1.5  $\text{Mo}_6\text{S}_8$  atomic layers (the bottom 0.5 layer frozen during optimization) was constructed to model the  $\text{Mo}_6\text{S}_8$  (001) surface and a vacuum spacing larger than  $10 \text{ \AA}$  was put on top of the slab to avoid interactions. The optimized bulk unit cell (Supplementary Fig. 24) has a lattice constant of  $6.50 \text{ \AA}$  that matches the experimental value very well<sup>66</sup>. The optimized geometry of the configuration of the pristine  $\text{Mo}_6\text{S}_8$  and the Li-intercalated  $\text{Mo}_6\text{S}_8$  ( $\text{LiMo}_6\text{S}_8$ ) is shown in Supplementary Fig. 25. To simulate the  $\text{Li}_1\text{Mo}_6\text{S}_8$  in our experiment, Li atoms are intercalated into the spacious sites surrounded by four  $\text{Mo}_6\text{S}_8$  clusters, which is in agreement with typical metallic ion intercalation in Chevrel-phase  $\text{Mo}_6\text{S}_8$  determined by both experiment and computation<sup>67</sup>.

The binding energy ( $E_b$ ) is defined as the difference between the total energy of the  $\text{Li}_2\text{S}_4$ -adsorbed system ( $E_{\text{total}}$ ), and the energy sum of isolated  $\text{Li}_2\text{S}_4$  and a clean  $\text{Mo}_6\text{S}_8$  surface (with or without Li intercalation):

$$E_b \equiv E_{\text{Li}_2\text{S}_4} + E_{\text{surface}} - E_{\text{total}} \quad (6)$$

A larger value indicates greater adsorbing ability.

## Data availability

The data that support the plots in this paper and other findings of this study are available from the corresponding author on reasonable request.

Received: 2 November 2017; Accepted: 11 February 2019;

Published online: 25 March 2019

## References

- Liu, X., Huang, J. Q., Zhang, Q. & Mai, L. Nanostructured metal oxides and sulfides for lithium-sulfur batteries. *Adv. Mater.* **29**, 1601759 (2017).
- Manthiram, A., Fu, Y., Chung, S. H., Zu, C. & Su, Y. S. Rechargeable lithium-sulfur batteries. *Chem. Rev.* **114**, 11751–11787 (2014).
- Zhang, S., Zhao, K., Zhu, T. & Li, J. Electrochemomechanical segregation of high-capacity battery electrode materials. *Prog. Mater. Sci.* **89**, 479–521 (2017).

4. Pang, Q., Liang, X., Kwok, C. Y., Kulisch, J. & Nazar, L. F. A comprehensive approach toward stable lithium-sulfur batteries with high volumetric energy density. *Adv. Energy Mater.* **7**, 1601630 (2016).
5. Xue, W. et al. Gravimetric and volumetric energy densities of lithium-sulfur batteries. *Curr. Opin. Electrochem.* **6**, 92–99 (2017).
6. Fan, F. Y. et al. Solvent effects on polysulfide redox kinetics and ionic conductivity in lithium-sulfur batteries. *J. Electrochem. Soc.* **163**, A3111–A3116 (2016).
7. Pang, Q., Liang, X., Kwok, C. Y. & Nazar, L. F. Advances in lithium-sulfur batteries based on multifunctional cathodes and electrolytes. *Nat. Energy* **1**, 16132 (2016).
8. Chen, J. et al. Improving lithium-sulfur battery performance under lean electrolyte through nanoscale confinement in soft swellable gels. *Nano Lett.* **17**, 3061–3067 (2017).
9. McCloskey, B. D. Attainable gravimetric and volumetric energy density of Li-S and Li-ion battery cells with solid separator-protected Li metal anodes. *J. Phys. Chem. Lett.* **6**, 4581–4588 (2015).
10. Choi, J. W. & Aurbach, D. Promise and reality of post-lithium-ion batteries with high energy densities. *Nat. Rev. Mater.* **1**, 16013 (2016).
11. Berg, E. J., Villeville, C., Streich, D., Trabesinger, S. & Novák, P. Rechargeable batteries: grasping for the limits of chemistry. *J. Electrochem. Soc.* **162**, A2468–A2475 (2015).
12. Ji, X., Evers, S., Black, R. & Nazar, L. F. Stabilizing lithium-sulphur cathodes using polysulphide reservoirs. *Nat. Commun.* **2**, 325 (2011).
13. Xue, W. et al. Double-oxide sulfur host for advanced lithium-sulfur batteries. *Nano Energy* **38**, 12–18 (2017).
14. Tao, X. et al. Strong sulfur binding with conducting Magneli-phase  $\text{Ti}_{(n)}\text{O}_{2(n-1)}$  nanomaterials for improving lithium-sulfur batteries. *Nano Lett.* **14**, 5288–5294 (2014).
15. Wei Seh, Z. et al. Sulphur-TiO<sub>2</sub> yolk-shell nanoarchitecture with internal void space for long-cycle lithium-sulphur batteries. *Nat. Commun.* **4**, 1331 (2013).
16. Liang, X. & Nazar, L. F. In situ reactive assembly of scalable core-shell sulfur-MnO<sub>2</sub> composite cathodes. *ACS Nano* **10**, 4192–4198 (2016).
17. Li, Z., Zhang, J. & Lou, X. W. Hollow carbon nanofibers filled with MnO<sub>2</sub> nanosheets as efficient sulfur hosts for lithium-sulfur batteries. *Angew. Chem. Int. Ed.* **54**, 12886–12890 (2015).
18. Liang, X. et al. A highly efficient polysulfide mediator for lithium-sulfur batteries. *Nat. Commun.* **6**, 5682 (2015).
19. Ma, L. et al. Hybrid cathode architectures for lithium batteries based on TiS<sub>2</sub> and sulfur. *J. Mater. Chem. A* **3**, 19857–19866 (2015).
20. Su, Y.-S. & Manthiram, A. Sulfur/lithium-insertion compound composite cathodes for Li-S batteries. *J. Power Sources* **270**, 101–105 (2014).
21. Zhou, G. et al. Catalytic oxidation of Li<sub>2</sub>S on the surface of metal sulfides for Li-S batteries. *Proc. Natl Acad. Sci. USA* **114**, 840–845 (2017).
22. Lin, Z., Liu, T. F. P., A. X. & Liang, C. D. Aligning academia and industry for unified battery performance metrics. *Nat. Commun.* **9**, 5262 (2018).
23. Zhao, Q., Zheng, J. & Archer, L. Interphases in lithium-sulfur batteries: toward deployable devices with competitive energy density and stability. *ACS Energy Lett.* **3**, 2104–2113 (2018).
24. Pan, H. et al. Addressing passivation in lithium-sulfur battery under lean electrolyte condition. *Adv. Funct. Mater.* **28**, 1707234 (2018).
25. Wang, H. et al. Tailored reaction route by micropore confinement for Li-S batteries operating under lean electrolyte conditions. *Adv. Energy Mater.* **8**, 1800590 (2018).
26. Chung, S. H. & Manthiram, A. Rational design of statically and dynamically stable lithium-sulfur batteries with high sulfur loading and low electrolyte/sulfur ratio. *Adv. Mater.* **30**, 1705951 (2018).
27. Mao, Y. et al. Foldable interpenetrated metal-organic frameworks/carbon nanotubes thin film for lithium-sulfur batteries. *Nat. Commun.* **8**, 14628 (2017).
28. Chung, S.-H. & Manthiram, A. Designing lithium-sulfur cells with practically necessary parameters. *Joule* **2**, 710–724 (2018).
29. Bai, S., Liu, X., Zhu, K., Wu, S. & Zhou, H. Metal-organic framework-based separator for lithium-sulfur batteries. *Nat. Energy* **1**, 16094 (2016).
30. Xu, G. et al. Absorption mechanism of carbon-nanotube paper-titanium dioxide as a multifunctional barrier material for lithium-sulfur batteries. *Nano Res.* **8**, 3066–3074 (2015).
31. Wang, X. et al. Structural and chemical synergistic encapsulation of polysulfides enables ultralong-life lithium-sulfur batteries. *Energy Environ. Sci.* **9**, 2533–2538 (2016).
32. Peng, H. J. et al. Healing high-loading sulfur electrodes with unprecedented long cycling life: spatial heterogeneity control. *J. Am. Chem. Soc.* **139**, 8458 (2017).
33. Zhou, G. et al. A graphene foam electrode with high sulfur loading for flexible and high energy Li-S batteries. *Nano Energy* **11**, 356–365 (2015).
34. Zhang, Q. et al. Understanding the anchoring effect of two-dimensional layered materials for lithium-sulfur batteries. *Nano Lett.* **15**, 3780–3786 (2015).
35. Yuan, Z. et al. Powering lithium-sulfur battery performance by propelling polysulfide redox at sulfiphilic hosts. *Nano Lett.* **16**, 519–527 (2016).
36. Zang, J. et al. Hollow-in-hollow carbon spheres with hollow foam-like cores for lithium-sulfur batteries. *Nano Res.* **8**, 2663–2675 (2015).
37. Li, G. et al. Chemisorption of polysulfides through redox reactions with organic molecules for lithium-sulfur batteries. *Nat. Commun.* **9**, 705 (2018).
38. Pan, H. et al. Non-encapsulation approach for high-performance Li-S batteries through controlled nucleation and growth. *Nat. Energy* **2**, 813 (2017).
39. Tan, G. et al. Burning lithium in CS<sub>2</sub> for high-performing compact Li<sub>2</sub>S-graphene nanocapsules for Li-S batteries. *Nat. Energy* **2**, 17090 (2017).
40. Levi, M. D. et al. Kinetic and thermodynamic studies of Mg<sup>2+</sup> and Li<sup>+</sup> ion insertion into the Mo<sub>6</sub>S<sub>8</sub> Chevrel phase. *J. Electrochem. Soc.* **151**, A1044 (2004).
41. Suo, L. et al. ‘Water-in-salt’ electrolyte enables high-voltage aqueous lithium-ion chemistries. *Science* **350**, 938–943 (2015).
42. Mei, L. et al. Chevrel phase Mo<sub>6</sub>T<sub>8</sub> (T = S, Se) as electrodes for advanced energy storage. *Small* **13**, 1701441 (2017).
43. Saha, P. et al. A convenient approach to Mo<sub>6</sub>S<sub>8</sub> Chevrel phase cathode for rechargeable magnesium battery. *J. Electrochem. Soc.* **161**, A593–A598 (2014).
44. Peng, H.-J., Huang, J.-Q., Cheng, X.-B. & Zhang, Q. Review on high-loading and high-energy lithium-sulfur batteries. *Adv. Energy Mater.* **7**, 1700260 (2017).
45. Cañas, N. A., Fronczek, D. N., Wagner, N., Latz, A. & Friedrich, K. A. Experimental and theoretical analysis of products and reaction intermediates of lithium-sulfur batteries. *J. Phys. Chem. C* **118**, 12106–12114 (2014).
46. Rajput, N. N. et al. Elucidating the solvation structure and dynamics of lithium polysulfides resulting from competitive salt and solvent interactions. *Chem. Mater.* **29**, 3375–3379 (2017).
47. Pope, M. A. & Aksay, I. A. Structural design of cathodes for Li-S batteries. *Adv. Energy Mater.* **5**, 1500124 (2015).
48. Hagen, M. et al. Lithium-sulfur cells: the gap between the state-of-the-art and the requirements for high energy battery cells. *Adv. Energy Mater.* **5**, 1401986 (2015).
49. Eroglu, D., Zavadil, K. R. & Gallagher, K. G. Critical link between materials chemistry and cell-level design for high energy density and low cost lithium-sulfur transportation battery. *J. Electrochem. Soc.* **162**, A982–A990 (2015).
50. Suo, L. et al. Fluorine-donating electrolytes enable highly reversible 5-V-class Li metal batteries. *Proc. Natl Acad. Sci. USA* **115**, 1156–1161 (2018).
51. Perdew, J. P., Burke, K. & Ernzerhof, M. Generalized gradient approximation made simple. *Phys. Rev. Lett.* **77**, 3865 (1996).
52. Blöchl, P. E. Projector augmented-wave method. *Phys. Rev. B* **50**, 17953 (1994).
53. Kresse, G. & Furthmüller, J. Efficient iterative schemes for ab initio total-energy calculations using a plane-wave basis set. *Phys. Rev. B* **54**, 11169 (1996).
54. Tkatchenko, A. & Scheffler, M. Accurate molecular van der Waals interactions from ground-state electron density and free-atom reference data. *Phys. Rev. Lett.* **102**, 073005 (2009).
55. Wan, L. F., Perdue, B. R., Applett, C. A. & Prendergast, D. Mg desolvation and intercalation mechanism at the Mo<sub>6</sub>S<sub>8</sub> Chevrel phase surface. *Chem. Mater.* **27**, 5932–5940 (2015).
56. Tarascon, J., DiSalvo, F., Murphy, D., Hull, G. & Waszczak, J. New superconducting ternary molybdenum chalcogenides in Mo<sub>6</sub>Se<sub>8</sub>, T<sub>1</sub>Mo<sub>5</sub>Se<sub>8</sub>, and T<sub>1</sub>Mo<sub>4</sub>Se<sub>8</sub>. *Phys. Rev. B* **29**, 172 (1984).
57. Geng, L., Lv, G., Xing, X. & Guo, J. Reversible electrochemical intercalation of aluminum in Mo<sub>6</sub>S<sub>8</sub>. *Chem. Mater.* **27**, 4926–4929 (2015).

## Acknowledgements

We acknowledge the support by Samsung Advanced Institute of Technology, National Key Technologies R&D Program, China (grant no. 2018YFB0104400) and the National Natural Science Foundation of China (grant no. 51872322). We also acknowledge the valuable suggestions for experiments from L. Miao and the carbonaceous materials provided by B. Fugetsu at School of Engineering, The University of Tokyo. This work made use of the MRSEC Shared Experimental Facilities supported by the National Science Foundation under award no. DMR-1419807. L.S. acknowledges the One Hundred Talent Project of the Chinese Academy of Sciences and Thousand Talents Program for Young Scientists.

## Author contributions

L.S., W.X. and J.L. conceived and designed the experiments. W.X., L.S. and C.W. fabricated the HMSC cathode. W.X., K.P.S., Y.C., L.Q., Z.Z. and G.X. carried out material characterization and electrochemical measurements. Z.S. carried out the DFT theoretical calculations. Z.W. and D.Y. carried out the TEM observation. H.W. and J.K. conducted the four-point-probe resistivity test. W.X., C.W. and A.M. made the pouch cell. W.X., L.S., J.L. and Z.S. wrote the paper. All authors discussed the results and reviewed the manuscript.

## Competing interests

The authors declare no competing interests.

## Additional information

Supplementary information is available for this paper at <https://doi.org/10.1038/s41560-019-0351-0>.

Reprints and permissions information is available at [www.nature.com/reprints](http://www.nature.com/reprints).

Correspondence and requests for materials should be addressed to L.S. or J.L.

**Publisher's note:** Springer Nature remains neutral with regard to jurisdictional claims in published maps and institutional affiliations.

© The Author(s), under exclusive licence to Springer Nature Limited 2019